2021

A Deblurring/Denoising Corrected Scintigraphic Planar Image Reconstruction Model for Targeted Alpha Theory

Charles Ross Schmidtlein
Memorial Sloan-Kettering Cancer Ctr.

Matthew Maroun
Columbia Univ.

Andrzej Krol
SUNY Upstate Medical University

Howard Gifford
University of Houston

Lisa Bodei
Memorial Sloan-Kettering Cancer Ctr.

See next page for additional authors

Original Publication Citation

Charles Ross, S., Matthew, M., Andrzej, K., Howard, G., Lisa, B., Joseph, O. D., Ida, H., Yuesheng, X., & Si, L. (2021). A deblurring/denoising corrected scintigraphic planar image reconstruction model for targeted alpha therapy, In *Medical Imaging 2021: Biomedical Applications in Molecular, Structural, and Functional Imaging*, edited by Barjor S. Gimi, Andrzej Krol, Proceedings of SPIE Vol. 11600 (SPIE, Bellingham, WA, 2021) 1160013. https://doi.org/10.1117/12.2584736

A deblurring/denoising corrected scintigraphic planar image reconstruction model for targeted alpha therapy

C. Ross Schmidtlein[a], Matthew Maroun[b], Andrzej Krol[c], Howard Gifford[d], Si Li[e], Lisa Bodei[a], Joesph O'Donoghue[a], Ida Häggström[a], and Yuesheng Xu[f]

[a]Memorial Sloan Kettering Cancer Center, 1250 First Avenue, New York City, NY, USA
[b]Columbia University, 535 W 116th Street, New York City, NY, USA
[c]State University of New York Upstate Medical University, 750 East Adams Street, Syracuse, NY, USA
[d]University of Houston, Houston, TX, USA
[e]Guangdong University of Technology, Guangzhou, China
[f]Old Dominion University, Norfolk, VA, USA

ABSTRACT

Scintigraphy is a common nuclear medicine method to image molecular target's bio-distribution and pharmacokinetics through the use of radiotracers and gamma cameras. The patient's images are obtained by using a pair of opposing large flat gamma ray detectors equipped with parallel-hole lead or tungsten collimators that preferentially detect gamma-rays that are emitted perpendicular to the plane of the detector. The resulting images form an anterior/posterior (A/P) planar image pairs. The obtained images are contaminated by noise and contain artifacts caused by gamma-ray attenuation, collimator penetration, scatter and other detrimental factors. Post-filtering of the images can reduce the noise, but at the cost of spatial resolution loss, and cannot remove any of the aforementioned artifacts. In this study, we introduced a new image reconstruction-based method to recover a single corrected planar scintigraphic patient image corrected for attenuation, system spatial resolution and collimator penetration, using the A/P image pair (two conjugated views) as data. To accomplish this task, we used a system model based on the gamma camera detectors physical properties and applied regularization method based on sparse image representation to control noise while preserving spatial resolution. In this proof-of-concept study, we evaluated the proposed approach using simple numerical phantoms. The images were evaluated for simulated lesions images contrast and background variability. Our initial results indicate that the proposed method outperforms the conventional methods. We conclude, that the proposed approach is a promising methodology for improved planar scintigraphic image quality and warrants further exploration.

Keywords: planar scintigraphic imaging, image reconstruction, sparse regularization

1. INTRODUCTION

In planar scintigraphy, radiologists and physicians view images of the accumulated count distribution produced by collimated single gamma photon emissions within a patient, typical anterior/posterior (A/P) pair. Unlike reconstructed 3D tomographic images, these images are not corrected for degradation due to physical processes such as attenuation, scatter, or collimator penetration. Thus, these images are not quantitative and many of the details are obscured by overlying structures.

This kind of imaging is especially problematic for high energy, low intensity gamma emission lines. This is especially problematic in the field of targeted alpha therapy (TAT) imaging. Another problem stems from half-lives of alpha emitting isotopes that results in high effective doses to patients and limits the acceptable administered activity of TAT. Nonetheless, it is vitally important to image the bio-distribution of TAT tracers to determine their therapeutic benefit and toxicity. In this situation the old adage of nuclear medicine physicians, ".. we want to treat what we see and see what we treat ...," takes on a new sense urgency.

Further author information: (Send correspondence to C. Ross Schmidtlein)
C. Ross Schmidtlein: E-mail: schmidtr@mskcc.org, Telephone: 1 212 639 8082

Medical Imaging 2021: Biomedical Applications in Molecular, Structural, and Functional Imaging, edited by Barjor S. Gimi, Andrzej Krol, Proc. of SPIE Vol. 11600, 1160013 · © 2021 SPIE
CCC code: 1605-7422/21/$21 · doi: 10.1117/12.2584736

A number of approaches have been used to improve planar scintigraphy images including denoising by post-filtering via a wavelet transformation,[1–8] a combination of Fourier and wavelet transformations,[9,10] contourlets,[6,11–13] bandelets,[6] complex ridgelets,[6,14] curvelets,[6,15,16] by more sophisticated blind-deconvolution schemes,[17] by statistically adaptive methods,[18–22] or by Monte Carlo methods,[23] but because these methods are not based on an underlying physical model they are incapable of removing image artifacts due to attenuation, scatter, or collimator penetration.

We observe that the physical model for planar scintigraphy is identical to two-views (A/P) single photon emission computed tomography (SPECT) system. Hence, if A/P planar images were fully corrected for noise and various artifacts and other degradation's, they would be identical. Unfortunately, the two-view SPECT physical model is severely ill-posed and cannot be used without additional considerations. We add that the geometric mean can partially correct attenuation, however, it does not remove other artifacts.

The goal of this research is to use the A/P views to produce a single combined, corrected planar scintigraphic image (CPSI). To do this, we propose a regularized image reconstruction approach that is based on a constrained two-view (A/P) SPECT physical model. In this approach, the two-view SPECT system model is used as a constraint to estimate the A/P projection of activity bio-distribution. This requires explicitly solving a highly ill-posed two-view SPECT problem. Because A/P views are co-linear there is very little depth information in the data, making 3D recovery problematic. However, because the information in the projection planes of the A/P images is preserved, the summing can still be performed and a CPSI can be recovered.

We hypothesize that this CPSI would be valuable tool for clinical application. We believe this will be especially true for challenging radionuclides such as those used in TAT. In the sections that follow, we will describe a CPSI reconstruction method based on a simplified two-view SPECT physical model, an effective regularization model, an efficient image reconstruction algorithm, and assess its performance in a simulated TAT imaging study.

2. METHODS

2.1 Corrected Planar Scintigraphic Image Integral Equations

The physical model for planar image formation is described by a two-view SPECT system model. To describe this model we begin by defining a region $J := [a, b]$ and its kernel as $K(\mathbf{x}; \mathbf{y})$ and data as $g(\mathbf{x})$, with $\mathbf{x}, \mathbf{y} \in J^3$. This results in the SPECT image reconstruction model as

$$\int_{J^3} K(\mathbf{x}; \mathbf{y}) f(\mathbf{y}) \, d\mathbf{y} = g(\mathbf{x}), \mathbf{x} \in J^3, \tag{1}$$

where $\mathbf{x} := (x_1, x_2, x_3)$ and $\mathbf{y} := (y_1, y_2, y_3)$.

In the case of the initial CPSI model, we define the projected activity distribution in y_3,

$$\overline{f}(y_1, y_2) := \int_J f(y_1, y_2, y_3) dy_3, \text{ subject to: eq. (1)}, \tag{2}$$

as the image we desire to recover. Introducing total variation regularization to control the noise this results in the following minimization problem

$$\begin{aligned} \overline{f}(y_1, y_2) = &\int_J f(y_1, y_2, y_3) dy_3, \text{ subject to:} \\ &\min_f \left\{ \left\| \int_{J^3} K(\cdot; \mathbf{y}) f(\mathbf{y}) d\mathbf{y} - g(\cdot) \right\|_{KL} + \lambda \|f\|_{TV(J^3)} + \iota_+(f) \right\}, \end{aligned} \tag{3}$$

where $\|\cdot\|_{KL}$ denotes the KL-divergence norm, λ is the regularization parameter, and ι_+ is the indicator function imposing a non-negativity constraint on f.

2.2 Idealized Kernel

Under the assumption of an ideal collimator and detectors, and a known attenuation map $\mu(\mathbf{y})$ with $\mathbf{y} \in J^3$, which can be provided by an accompanying CT, the kernel for the problem shown in (1) is given by

$$K(\mathbf{x};\mathbf{y}) = \delta(x_1 - y_1, x_2 - y_2) e^{-\int_{y_3}^{x_3} \mu(y_1,y_2,t)dt} + s(\mathbf{x}),\ \mathbf{x},\mathbf{y} \in J^3\,, \tag{4}$$

where $s(\mathbf{x})$ represents an additive term such as scatter that is independently estimated. This leads to the constrained integral formulation in equation (3) of the CSPI reconstruction model given by

$$\begin{aligned} &\overline{f}(y_1,y_2) = \int_J f(y_1,y_2,y_3)dy_3, \text{ subject to:} \\ &\min_f \left\{ \left\| \int_J e^{-\int_{y_3}^{x_3} \mu(y_1,y_2,t)dt} f(y_1,y_2,y_3)dy_3 + s(y_1,y_2) - g(y_1,y_2) \right\|_{KL} + \lambda \left\| f \right\|_{TV(J^3)} + \iota_+(f) \right\}. \end{aligned} \tag{5}$$

Discretizing this model where region J^3 gives

$$\overline{f} = \sum_{y_3} f(\mathbf{y}), \text{ subject to: } \min_f \left\{ \left\| Kf + s - g \right\|_{KL} + \lambda \left\| B_3 f \right\|_1 + \iota_+(f) \right\}, \tag{6}$$

Ignoring terms solely dependent on g the KL-divergence term in eq. (6) is given by

$$\left\| Kf + s - g \right\|_{KL} = Kf + s - g \log\left(Kf + s\right). \tag{7}$$

2.3 Fixed Point Algorithm

To solve the discretized idealized model (6) we use a preconditioned proximity gradient algorithm similar to that described in Lin et al.[24] This results in following fixed-point algorithm with higher order total variation (HOTV) regularization,[24–26]

$$\begin{cases} f^{k+1} = \text{prox}_{\iota_+}\left\{ f^k - S\left[K^\top \left(1 - \frac{g}{Kf^k + s} \right) + B_3^\top b^k + C_3^\top c^k \right] \right\} \\ b^{k+1} = \rho_1 (I - \text{prox}_{\frac{\lambda_1}{\rho_1}\varphi_1})(\frac{b^k}{\rho} + B_3(2f^{k+1} - f^k)) \\ c^{k+1} = \rho_2 (I - \text{prox}_{\frac{\lambda_2}{\rho_2}\varphi_2})(\frac{c^k}{\rho} + C_3(2f^{k+1} - f^k)), \end{cases} \tag{8}$$

where b^k and c^k are the respective subgradient terms, B_3 and C_3 the respective 3D first and second order gradient block matrices, $\varphi_{1,2}$ are the first and second order isotropic total variation norms, $\lambda_{1,2}$ are the regularization weights, S is the preconditioner, and $\rho_{1,2}$ are the algorithmic parameters. The Moreau envelope function for a convex function $\psi : \mathrm{R}^n \to \mathrm{R}$ is defined by

$$\text{prox}_\psi(x) = \arg\min_u \left\{ \frac{1}{2}\|u - x\|_2^2 + \psi(u) : u \in \mathrm{R}^n \right\}. \tag{9}$$

For the definitions of B_3 and C_3, we let $N = \sqrt{d}$, I_N denote the $N \times N$ identity matrix, D denote the $N \times N$ backward difference matrix such that $D_{j,j} = 1$ and $D_{j,j-1} = -1$ for $j = 2, 3, \ldots, N$, and all other entries of D are zero. Through the matrix Kronecker product $\otimes$, $B_3 \in \mathrm{R}^{3N}$ and $C_3 \in \mathrm{R}^{9N}$ are defined, respectively, by

$$B_3 := \begin{bmatrix} I_N \otimes I_N \otimes D \\ I_N \otimes D \otimes I_N \\ D \otimes I_N \otimes I_N \end{bmatrix}, C_3 := \begin{bmatrix} I_N \otimes I_N \otimes (-D^\top)D \\ I_N \otimes (-D^\top) \otimes D \\ (-D^\top) \otimes I_N \otimes D \\ I_N \otimes D \otimes (-D^\top) \\ I_N \otimes (-D^\top)D \otimes I_N \\ (-D^\top) \otimes D \otimes I_N \\ D \otimes I_N \otimes (-D^\top) \\ D \otimes (-D^\top) \otimes I_N \\ (-D^\top)D \otimes I_N \otimes I_n \end{bmatrix}. \tag{10}$$

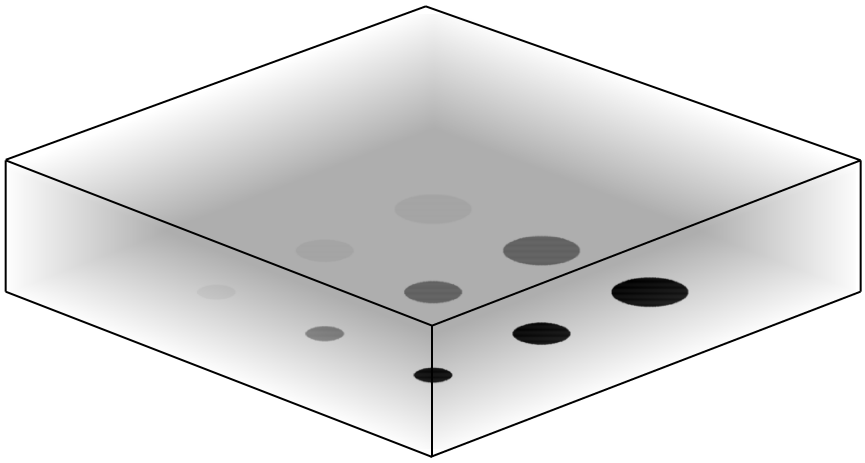

Figure 1: Maximum-Intensity Projection of the contrast detail phantom. Phantom size is 64 cm x 64 cm x 16 cm, with a 1-cm gap of air on all sides in the FOV.

The first and second order isotropic total variation norms are defined by

$$\varphi_1(x) = \sum_{i=1}^{d} \sqrt{\sum_{j=0}^{2} x_{i+jd}^2}\,, \quad \text{and} \quad \varphi_2(y) = \sum_{i=1}^{d} \sqrt{\sum_{j=0}^{8} y_{i+jd}^2}\,. \tag{11}$$

The preconditioner in eq. (8) S is defined by

$$S = \frac{f^k}{K^\top 1}\,. \tag{12}$$

The algorithmic parameter is taken from[26] and is defined by

$$\rho_{1,2} = \frac{1}{2\|B_3, C_3\|_2^2 \|S\|_\infty}\,, \tag{13}$$

where $\|B_3\|_2^2 = 12$ and $\|C_3\|_2^2 = 144$. The regularization weights $\lambda_{1,2}$ were determined by minimum mean squared error.

2.4 Simulation Description

To test our method, we reconstructed a numerical phantom with a 3x3 contrast detail object in a uniform background. The phantom, shown in Fig. 1, is a 64x64x16 cm^3 box with with grid of 1 cm thick discs with radii (2, 3, & 4) cm and intensity (1.75, 2.125, & 2.5) times the A/P background counts. The disks were inserted at a depth of 2 cm from posterior detector. An Actinium-225 source was used that included its short lived daughter products including Francium-221, Astatine-217, and Bismuth-213. Eight photon emissions were taken into account (all emissions with 1% or larger branching ratios) and are shown in Table 1. A 50% scatter background was used. We performed this reconstruction using 12500, 25000, and 50000 total counts using a HOTV penalty.

3. RESULTS

Figure 3 shows the results obtained with HOTV. On can see that the reconstructed corrected scintigraphic planar images are much smoother while still preserving lesion conspicuity. This is seen in both the single realization and is in the mean images of 200 realizations (not shown).

The recovered contrast versus background variability trade-off plots obtained from 200 realizations are shown in Fig. 4 at three count levels (12,500, 25,000, and 50,000 counts) with a 50% scatter fraction. In this figure, the reconstruction performance across a wide range of regularization weights and post-filter strengths are shown for the HOTV and geometric mean images, respectively.

Table 1: Photo-peak energies from the ^{225}Ac decay chain (^{225}Ac decay chain (^{225}Ac $\xrightarrow{t_{1/2}=9.92d}$ ^{221}Fr $\xrightarrow{t_{1/2}=4.8min}$ ^{217}At $\xrightarrow{t_{1/2}=33\mu s}$ ^{213}Bi $\xrightarrow{t_{1/2}=45.6min}$) considered for preliminary image simulation. The attenuation coefficient in lead at 99.91 keV is large due to the k-edge of lead around that energy. Horizontal lines within table contents represent the energy windows considered for imaging: 15 percent width window centered at 87 keV, 10 percent windows centered at 218 keV and 440 keV.

Emitting Nuclide	Photo-peak Energy (keV)	Branching Ratio	Fraction of Max. Branching Ratio	μ_{H_2O} (cm^{-1})	μ_{NaI} (cm^{-1})	μ_{Pb} (cm^{-1})
^{213}Bi	76.863	0.012	0.046	0.186	12.238	30.364
^{213}Bi	79.290	0.020	0.076	0.184	11.270	28.064
^{221}Fr	81.517	0.015	0.056	0.182	10.406	26.032
^{225}Ac	83.231	0.012	0.045	0.181	9.911	24.873
^{225}Ac	86.105	0.020	0.074	0.179	9.058	22.867
^{225}Ac	99.910	0.010	0.039	0.171	6.137	63.081
^{221}Fr	218.190	0.116	0.444	0.133	1.024	9.245
^{213}Bi	440.460	0.261	1.000	0.102	0.391	2.236

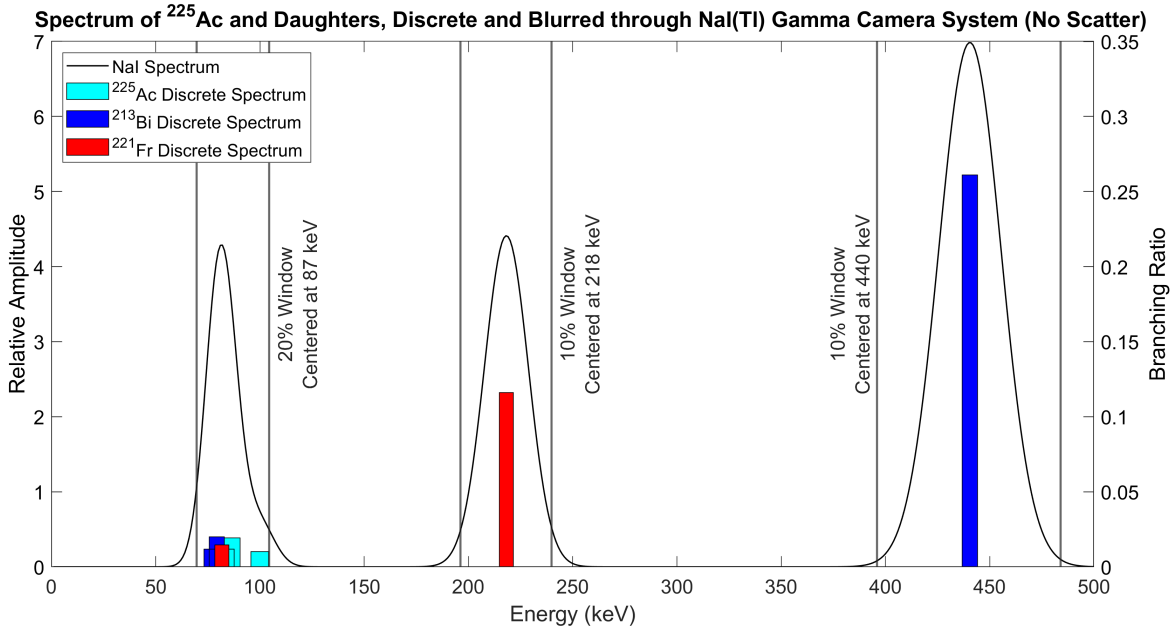

Figure 2: Energy resolution of NaI and spectrum of photopeaks from the ^{225}Ac decay chain, ^{225}Ac decay chain (^{225}Ac $\xrightarrow{t_{1/2}=9.92d}$ ^{221}Fr $\xrightarrow{t_{1/2}=4.8min}$ ^{217}At $\xrightarrow{t_{1/2}=33\mu s}$ ^{213}Bi $\xrightarrow{t_{1/2}=45.6min}$) with proposed energy windows to be used for imaging. Peaks, weighted with their respective branching ratios, are plotted according to the ratios found in Table 1. The resolution of the NaI gamma camera is calibrated at 6.5% at 662 keV, with a $1/\sqrt{E}$ energy dependence.[27]

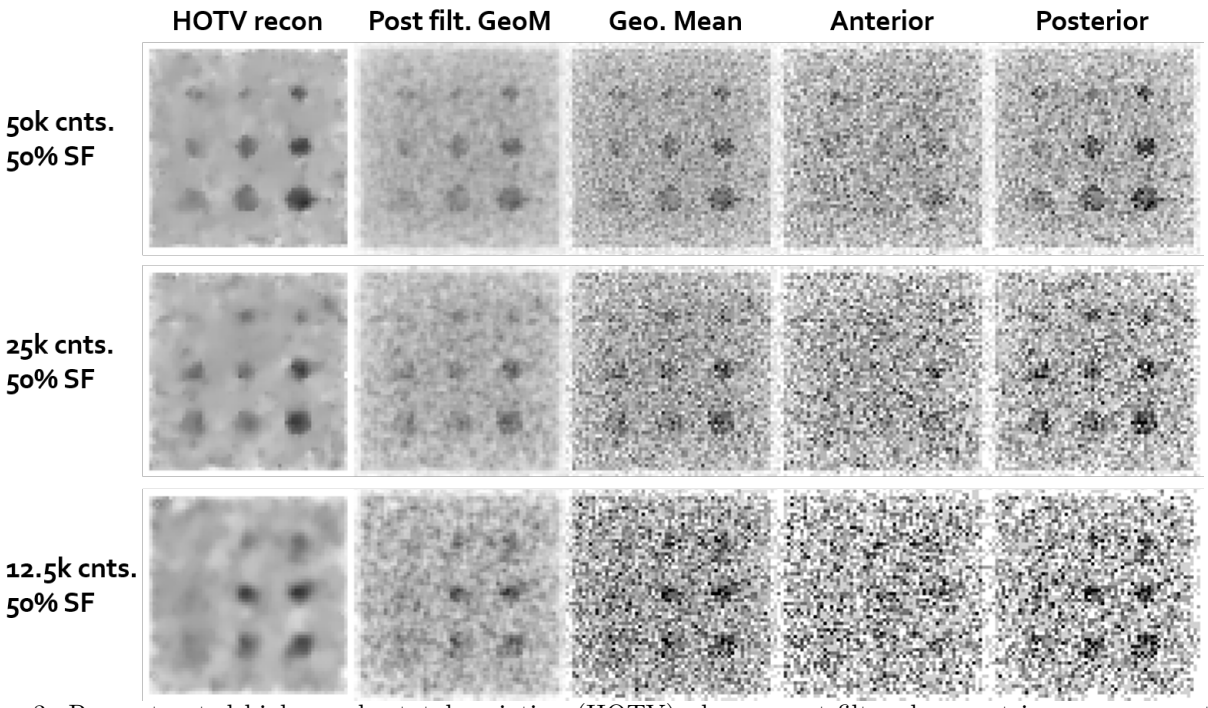

Figure 3: Reconstructed higher order total variation (HOTV) planar, post-filtered geometric mean, geometric mean, and A/P imagesare shown from left to right (1 of 200 realizations) at three count levels (12,500, 25,000, and 50,000 counts) with a 50% scatter fraction. The HOTV and post-filtered geometric mean images were optimized with respect to minimum mean squared error.

4. DISCUSSION

In this initial study, we used a highly idealized SPECT system model to test our planar image reconstruction method. The results here are promising, and we expect that more detailed system model that includes more realistic spatial resolution and collimator penetration modeling will show image quality additional improvement, as compared to uncorrected images. We also expect that a more advanced regularization model would lead to improvements over our HOTV model. It is our conjecture that our method will outperform post-processing methods that do not include a physical model of the imaging system in their attempts to denoise/deblur scintigraphic images.

5. CONCLUSIONS

We conclude our constrained integral approach produced better images, as compared to conventional geometric mean images. We show that our method better recovers contrast while suppressing image noise than a geometric mean image with post-filtering. However, we have not evaluated our method for detection tasks performance and we have not used it with patient images. The proposed corrected planar scintigraphic image reconstruction methods is an unexplored idea, with which the clinical utility has not yet been investigated. Here we present the first steps of a very promising idea that needs further exploration.

ACKNOWLEDGMENTS

The authors wish to thank James Keller in the Department of Medical Physics at Memorial Sloan Kettering Cancer Center for his help in editing the manuscript. Y. Xu is supported by US National Science Foundation under grant DMS-1912958 and by Natural Science Foundation of China under grant 11771464. C.R. Schmidtlein is supported in part by the MSK Cancer Center Support Grant/Core Grant (P30 CA008748).

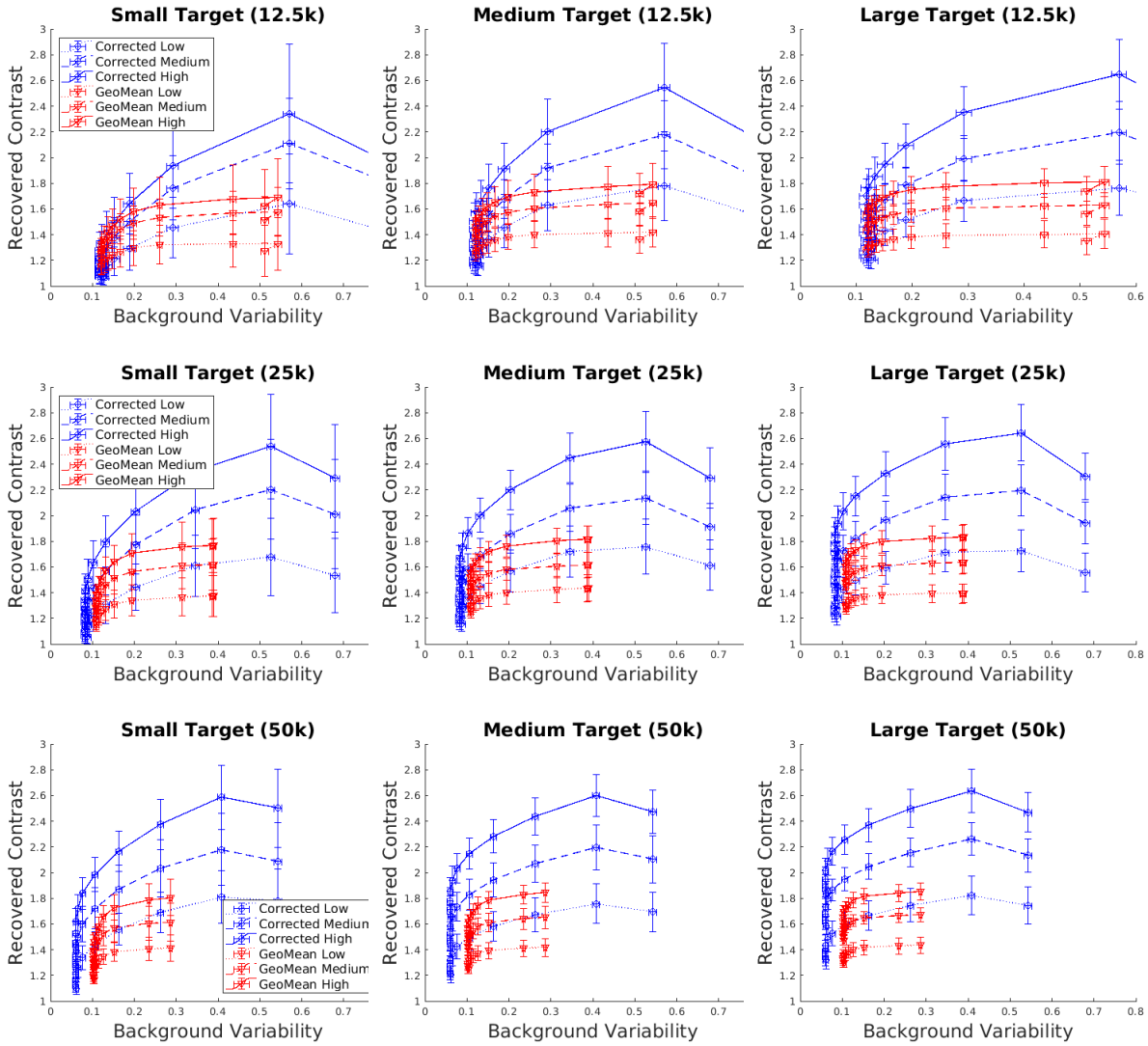

Figure 4: Recovered contrast / background variability trade-off plots from 200 realizations are shown at three count levels (12,500, 25,000, and 50,000 counts) using a 50% scatter fraction. Each target (small, medium, and large) are compared at three contrast levels.

REFERENCES

[1] Khlifa, N., Kamel, H., and Noureddine, E., "Image denoising using wavelets: A powerful tool to overcome some limitations in nuclear imaging," in [*Medical Imaging*], Brunet, G., ed., *Proc, ICTTA* **2**, 1114–1118 (2006).

[2] Arikidis, N., J., Kalatzis, Tsantis, S., Prassopoulos, V., and Cavouras, D., "Suppression of high frequency noise from scintigraphic images using the discrete wavelet transform," in [*European Symposium on Biomedical Engineering and Medical Physics*], **3**, 36 (2002).

[3] Kirkokve, M. and Seret, A., "Comparative study of wavelet packet local thresholdings within the framework of scintigraphic images denoising," *Experimental Medical Imaging* (2005).

[4] Gribaa, N., Khlifa, N., and Hamrouni, K., "Scintigraphic images restoration using jointly fourier and wavelet domains," in [*2008 3rd International Conference on Information and Communication Technologies: From Theory to Applications*], 1–5 (2008).

[5] Ogawa, K., Sakata, M., and Li, Y., "Adaptive noise reduction of scintigrams with a wavelet transform," *International Journal of Biomedical Imaging* **2012**, 7 pages (2012).

[6] Makhlouf, F., Besbes, H., N. Khlifa, C. B. A., and Solaiman, B., "Planar scintigraphic images denoising," *Open Journal of Medical Imaging* **3**, 116–124 (2013).

[7] Nowak, R. D. and Baraniuk, R. G., "Wavelet-domain filtering for photon imaging systems," *IEEE Transactions on Image Processing* **8**(5), 666–678 (1999).

[8] Khan, A. and Singh, M., "Wavelet transform based image denoising using different thresholding methods," in [4^{th} *ICCEE*], (2011).

[9] Guy, M. J., "Fourier block noise reduction: an adaptive filter for reducing poisson noise in scintigraphic images," *Nuclear Medicine Communications* **29**(3), 291–297 (2008).

[10] King, M. A., Doherty, P. W., Schwinger, R. B., and Penney, B. C., "A wiener filter for nuclear medicine images," *Medical Physics* **10**, 876–880 (1983).

[11] Zhang, X. and Jing, X., "Image denoising in contourlet domain based on a normal inverse gaussian prior," *Digital Signal Processing* **20**, 1439–1446 (2010).

[12] Li, X. M., Yan, G. P., and Chen, L., "A new method of image denoise using contourlet transform," *Intelligent Information Technology Application* **3**, 25–30 (2010).

[13] Chen, G. and Zhu, W., "Image denoising using neighboring contourlet coefficitents," in [*Proceeding of the* 5^{th} *International Symposium on Neural Networks: Advances in Neural Networks*], **5264**, 384–391 (2008).

[14] Chen, G. Y. and Kegl, B., "Image denoising with complex ridgelets," 1439–1446 (2006).

[15] Binh, N. T. and Khare, A., "Multilevel threshold-based image denoising in curvelet domain," *Computer Science and Technology* **25**, 632–640 (2010).

[16] Reddy, G. J., Prasad, T. J., and Prasad, M. N., "Fingerprint image denoising using curvelet transform," *Engineering and Applied Sciences* **3** (2008).

[17] Dupe, F. X., Fadili, J. M., and Starck, J. L., "A proximal iteration for deconvolving poisson noisy images using sparse representations," *IEEE Transactions on Image Processing* **18**(2), 310–321 (2009).

[18] Khan, K. B., Shahid, M., H. Ullah, E. R., and Khan, M. M., "Adaptive trimmed mean autoregressive model for reduction of poisson noise in scintigraphic images," *IIUM Engineering Journal* **19**(2), 68–79 (2018).

[19] Khan, K. B., Khaliq, A. A., Shahid, M., and Ullah, H., "Poisson noise reduction in scintigraphic images using gradient adaptive trimmed mean filter," in [*2016 International Conference on Intelligent Systems Engineering (ICISE)*], 301–305 (2016).

[20] Weselowski, C., Yahil, A., Puetter, R., Babyn, P., Gilday, D., and Khan, M., "Improved lesion detection from spatially adaptive, minimally complex, pixon® reconstruction of planar scintigraphic images," *Computational Medical Imaging Graph.* **29**, in press (2005).

[21] Vija, A., Gosnell, T., A. Yahil, E. H., and Engdahl, J., "Statistically based spatially adaptive noise reductin of planar nuclear studies," in [*SPIE Medical Imaging 2005: Image Processing*], *Proc. SPIE* **5747** (2005).

[22] Hannequin, P. and Mas, J., "Statistical and heuristic noise extraction (shine): a new method for processing poisson noise in scintigraphic images," *Physics in Medicine and Biology* **47**(24), 4329–4344 (2002).

[23] Minarik, D., Enqvist, O., and Tragardh, E., "Denoising of scintillation camera images using a deep convolutional neural network: a monte carlo simulation approach," *The Journal of Nuclear Medicine* **61**(2), 298–303 (2020).

[24] Lin, Y., Schmidtlein, C. R., Li, Q., Li, S., and Xu, Y., "A krasnoselskii-mann algorithm with an improved em preconditioner for pet image reconstruction," *IEEE transactions on medical imaging* **38**(9), 2114–2126 (2019).

[25] Schmidtlein, C. R., Lin, Y., Li, S., Krol, A., Beattie, B. J., Humm, J. L., and Xu, Y., "Relaxed ordered subset preconditioned alternating projection algorithm for pet reconstruction with automated penalty weight selection," *Medical physics* **44**(8), 4083–4097 (2017).

[26] Li, S., Zhang, J., Krol, A., Schmidtlein, C. R., Vogelsang, L., Shen, L., Lipson, E., Feiglin, D., and Xu, Y., "Effective noise-suppressed and artifact-reduced reconstruction of spect data using a preconditioned alternating projection algorithm," *Medical physics* **42**(8), 4872–4887 (2015).

[27] Knoll, G. F., [*Radiation Detection and Measurement*], Wiley, 111 River St. Hoboken, New Jersey (2010 (fourth edition)).